Mechanical Spin Control of Nitrogen-Vacancy Centers in Diamond

E. R. MacQuarrie, T. A. Gosavi, N. R. Jungwirth, S. A. Bhave, and G. D. Fuchs*
Cornell University, Ithaca, New York 14853, USA
(Received 4 July 2013; published 27 November 2013)

We demonstrate direct coupling between phonons and diamond nitrogen-vacancy (NV) center spins by driving spin transitions with mechanically generated harmonic strain at room temperature. The amplitude of the mechanically driven spin signal varies with the spatial periodicity of the stress standing wave within the diamond substrate, verifying that we drive NV center spins mechanically. These spin-phonon interactions could offer a route to quantum spin control of magnetically forbidden transitions, which would enhance NV-based quantum metrology, grant access to direct transitions between all of the spin-1 quantum states of the NV center, and provide a platform to study spin-phonon interactions at the level of a few interacting spins.

DOI: 10.1103/PhysRevLett.111.227602 PACS numbers: 76.30.Mi, 63.20.kp, 72.55.+s, 77.55.hd

As spin-based quantum technology evolves, the ability to manipulate spin with nonmagnetic fields could enable an interface for hybrid quantum systems and facilitate integration with conventional technology. Particularly useful examples are electric fields, optical fields, and mechanical lattice vibrations. The last of these represents direct spin-phonon coupling, which has garnered fundamental interest as a potential mediator of spin-spin interactions [1,2].

Nitrogen-vacancy (NV) center spins in diamond are a promising solid-state platform for quantum information science [3,4] and precision metrology. They are sensitive magnetometers [5,6], electrometers [7], and thermometers [8,9] with nanoscale spatial resolution due to their atomic size [10,11]. Significant progress in integrating NV centers with microelectromechanical systems (MEMS) has paved the way for studies of spins coupled to mechanical resonators [12–17]. In previous work, NV centers have been coupled to phonons indirectly, either by using a magnetic field gradient or by tuning the frequency of a magnetic spin transition. Here, we use a MEMS transducer to directly drive electronic spin transitions in NV centers using gigahertz-frequency mechanical (stress) waves. This work demonstrates direct spin-phonon interactions at room temperature as a means to drive magnetically forbidden spin transitions.

Driving spin transitions is the key to using NV center spins for quantum information science or sensing. Conventionally, quantum spin control in this system is accomplished with gigahertz-frequency magnetic fields [18–20] or with optical fields at cryogenic temperatures [21]. Resonant lattice vibrations couple to nuclear quadrupole moments [22] and represent another avenue to manipulate NV center electronic spins. NV centers couple to a magnetic field ($B_\parallel$ and $B_\perp$) and a stress ($\sigma_\parallel$ and $\sigma_\perp$) through their ground-state spin Hamiltonian [7,23]

$$H_{\mathrm{NV}} = (D_0 + \epsilon_\parallel \sigma_\parallel) S_z^2 + \gamma_{\mathrm{NV}} B_\parallel S_z + \gamma_{\mathrm{NV}} B_\perp S_x - \epsilon_\perp \sigma_x (S_x^2 - S_y^2) + \epsilon_\perp \sigma_y (S_x S_y + S_y S_x), \quad (1)$$

where $D_0 = 2.87$ GHz is the zero-field splitting, $\gamma_{\mathrm{NV}} = 2.8$ MHz/G is the gyromagnetic ratio, $\epsilon_\perp = 0.03$ MHz/MPa [1,24] and $\epsilon_\parallel$ are the perpendicular and axial stress coupling constants, and S_x, S_y, S_z are the x, y, and z components of the spin-1 operator, respectively. The z axis is defined along the NV symmetry axis as depicted in Fig. 1(a).

In the S_z basis, H_{NV} has eigenstates $\{|(m_s =)0\rangle, |+1\rangle, |-1\rangle\}$. D_0 breaks the degeneracy between the $|0\rangle$ and $|\pm 1\rangle$ spin states at zero magnetic field. Careful alignment of a static external magnetic field $B_\parallel$ along the NV

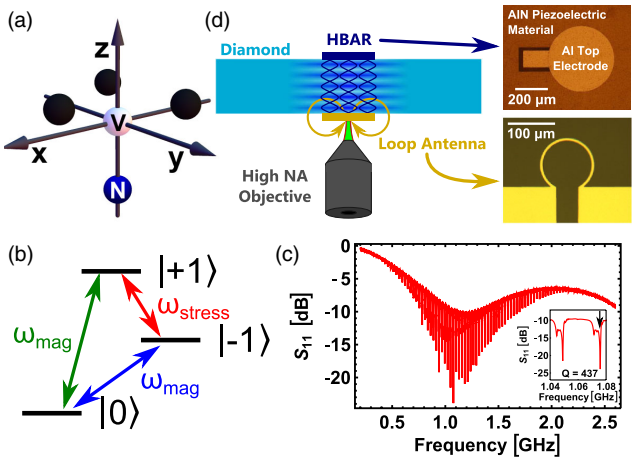

FIG. 1 (color online). (a) Schematic of an NV center. The z axis corresponds to the symmetry axis of the NV center. (b) Levels of an NV center ground-state spin. Magnetic driving enables $\Delta m_s = \pm 1$ transitions, whereas mechanical driving can produce $\Delta m_s = \pm 2$ transitions. (c) Reflected microwave power (S_{11}) as a function of frequency from the MEMS device measured using a network analyzer. Standing wave resonances have Qs as high as 437. (d) Device schematic. A loop antenna produces gigahertz-frequency magnetic fields for magnetic control while an HBAR produces gigahertz-frequency stress standing waves within the diamond.

symmetry axis zeros the static component of $B_\perp$ and splits the $|+1\rangle$ and $|-1\rangle$ states. For conventional magnetic spin driving, an oscillating $B_\perp$ can drive spin transitions from the $|0\rangle$ state to either the $|+1\rangle$ or the $|-1\rangle$ state. Similarly, a perpendicular stress couples the $|+1\rangle$ and $|-1\rangle$ states, allowing a direct $|+1\rangle \leftrightarrow |-1\rangle$ spin transition to be driven by a gigahertz-frequency stress wave resonant with the spin-state splitting. In the S_z basis, this transition is magnetically forbidden by the magnetic dipole selection rule, $\Delta m_s = \pm 1$. Thus, the ability to drive $|+1\rangle \leftrightarrow |-1\rangle$ with an oscillating stress wave and $|0\rangle \leftrightarrow |\pm 1\rangle$ with oscillating magnetic fields establishes direct transitions between all three spin levels, as depicted in Fig. 1(b). Additionally, an axial stress $\sigma_\parallel$ shifts $|+1\rangle$ and $|-1\rangle$ equivalently and, therefore, has no effect on mechanical spin control performed in the $|\pm 1\rangle$ spin subspace.

The stress coupling coefficient $\epsilon_\perp$ is small enough that a large stress is required to produce a driving field comparable to those achieved with magnetic fields. To drive a large stress resonant with gigahertz-frequency spin transitions, we fabricated high-overtone bulk acoustic resonators (HBARs) [25] on one face of a 300 μm thick, $\langle 100 \rangle$ diamond [26]. The type IIa diamond used in these measurements is dense with native NV centers ($\approx 3 \times 10^{14}$ NV/cm^3), placing ≈ 230 NVs inside the confocal volume of our microscope. These NV centers are randomly oriented along one of the four $\langle 111 \rangle$ crystal axes within the diamond. By aligning the static magnetic field $B_\parallel$ with one such axis, we isolate a single NV species from the four possible orientations, leaving ≈ 58 NVs that contribute to the signal in our experiments. Those NV centers that are not aligned with $B_\parallel$ are not resonant with our control pulses so their fluorescence contributes a constant background to our measurements that is subtracted during data processing.

The HBAR consists of a 3 μm thick aluminum nitride (AlN) piezoelectric film sandwiched between two 400 μm diameter metal electrodes. Applying a gigahertz-frequency voltage across the AlN launches a longitudinal stress wave into the diamond. The diamond substrate acts as an acoustic Fabry-Pérot cavity, generating stress standing wave resonances with a pitch determined by the speed of sound in the diamond and the substrate thickness. By measuring the microwave power reflected from the device (S_{11}), we observed the resonant frequency comb of an HBAR [Fig. 1(c)]. From this data, we used the Q-circle method [27] to find that the unloaded quality factor (Q) of each resonance, which is as high as $Q = 437$ for $\omega_{\mathrm{HBAR}} = 2\pi \times 1.076$ GHz. Based on a one-dimensional oscillator model [28], this corresponds to a stress of $\sigma_{\mathrm{max}} \approx 10$ MPa directed along the [001] crystal axis of the diamond for 25 dBm of applied microwave power. By transforming the resulting stress tensor from the lattice coordinates to the coordinates of the NV center, we estimate the applied perpendicular stress to be $\sigma_\perp \approx 7$ MPa [26]. This is enough for an $\Omega_{\mathrm{stress}} \approx 2\pi \times 210$ kHz spin driving field. On the opposite face of the diamond, we fabricated a loop antenna for magnetic spin control [Fig. 1(d)].

To demonstrate mechanical spin control, we performed optically detected mechanical spin resonance (ODMSR) measurements of the $|-1\rangle \rightarrow |+1\rangle$ spin transition. The pulse sequences used for this experiment are shown in Fig. 2(a). First, the NV center ensemble is initialized into $|0\rangle$ by optical pumping with a 532 nm laser. The laser is then turned off and a magnetic adiabatic passage through the $|0\rangle \rightarrow |-1\rangle$ resonance robustly transfers the initialized spin population into the $|-1\rangle$ state [26,29]. The stress wave is then turned on for 6 μs at a frequency ω_{HBAR} corresponding to a resonance of the HBAR. Pulsing the stress wave ensures that any axial stress generated by the HBAR has no effect on the $|0\rangle \leftrightarrow |-1\rangle$ magnetic driving. After this stress pulse, a second magnetic adiabatic passage transfers the population remaining in $|-1\rangle$ to the $|0\rangle$ state. Fluorescence read out of the population in the $|0\rangle$ state is then performed, giving the signal for the experiment. Fluorescence read out is also performed after initialization into the $|0\rangle$ state to provide normalization for each iteration of the duty cycle. By repeating this sequence as a function of $B_\parallel$, we scan $\omega_{\pm 1}$, the energy splitting between $|+1\rangle$ and $|-1\rangle$. Whenever $\omega_{\pm 1} = \omega_{\mathrm{HBAR}}$, the strain pulse transfers population from $|-1\rangle$ to $|+1\rangle$. Population transferred to $|+1\rangle$ during the stress pulse shows up as missing population in $|0\rangle$ via fluorescence measurement at the end of the duty cycle.

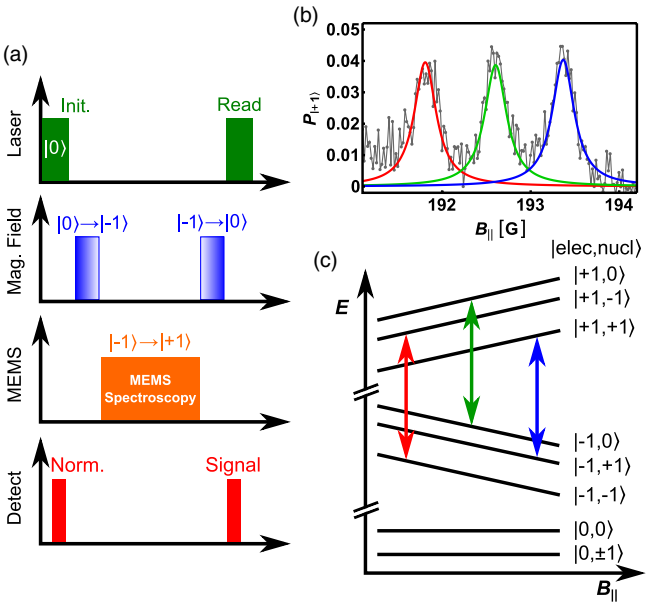

FIG. 2 (color online). (a) Pulse sequence used for ODMSR measurements. (b) Population driven into the $|+1\rangle$ state by the mechanical driving field as a function of the axial magnetic field $B_\parallel$ for $\omega_{\mathrm{HBAR}} = 2\pi \times 1.076$ GHz at room temperature. (c) NV hyperfine structure labeled with the experimentally observed transitions. Each arrow corresponds with the resonance condition $\omega_{\pm 1} = \omega_{\mathrm{HBAR}}$ for each of the three nuclear spin sublevels.

Typical ODMSR results are shown in Fig. 2(b). The spectrum shows three peaks with 0.78 ± 0.02 G spacing. This corresponds to the $A/\gamma_{NV} = 0.77$ G hyperfine splitting arising from interactions between the NV spins and the unpolarized nuclear spins of the ^{14}N atoms neighboring the vacancies [23,26]. Because the nuclear spins are not polarized, only one third of the spins are resonant with each hyperfine sublevel, which reduces the contrast by a factor of 3. The contrast is also reduced by inhomogeneous mechanical driving of the NV ensemble. To account for dephasing and inhomogeneous driving, we calibrate the spin contrast by driving with conventional magnetic spin resonance [26]. For the resonance at $\omega_{HBAR} = 2\pi \times 1.076$ GHz, we estimate the peak mechanical driving field is $\Omega_{stress} \approx 2\pi \times 230$ kHz. This is consistent with the coupling strength of 0.03 MHz/MPa, which was previously determined from measurements of static strain at low temperature [1,24]. For scale, a single NV with a polarized nuclear spin driven at a stress antinode of this resonance would show 14% spin contrast. We also verified that the spin contrast scales with the mechanical Q by measuring ODMSR at an HBAR resonance with a different Q [26].

Because stress and electric fields enter the NV spin Hamiltonian in the same way [23], we verified that the ODMSR signals do not result from stray electric fields. To address this possibility, we used the finite element analysis software ANSYS HFSS to simulate the electric field generated during the stress pulse, which comprises the dominant source of stray electric fields in the experiment. The loop antenna on the rear face of the diamond was included. The simulated electric field within the relevant region of the diamond was no larger than $E_{sim} = 10$ V/cm. The coupling strength between a perpendicular electric field and the NV ground state spin is $d_{gs}^{\perp} = 17 \pm 3$ Hz cm/V [7,30]. Under conservative assumptions, E_{sim} would generate a driving field roughly 3 orders of magnitude lower than observed in the experiment. We also considered, but ruled out, magnetic driving of the $|+1\rangle \leftrightarrow |-1\rangle$ transition via stray magnetic fields from the MEMS transducer [26].

As a critical verification that we drive spin transitions with mechanically generated stress waves, we investigated how the ODMSR signal varies as a function of depth. Because we drive a stress standing wave, we expect that the ODMSR signal will be modulated at the periodicity of the standing wave. Taking care to account for optical aberrations introduced from refraction at the air-diamond interface [31], we repeated ODMSR measurements of the $\omega_{HBAR} = 2\pi \times 0.942$ GHz mechanical resonance at different depths within the sample. To correctly interpret the results, we note that our microscope collects fluorescence from all of the NV centers within its confocal volume. Figure 3(a) depicts schematically the variation in stress amplitude across an approximate confocal point spread function (PSF). Different regions within the confocal volume experience different stress driving fields, and we sample the range of stresses within the PSF. This reduces the spatial resolution in the focal direction and contributes to the inhomogeneous spin dephasing of the NV centers.

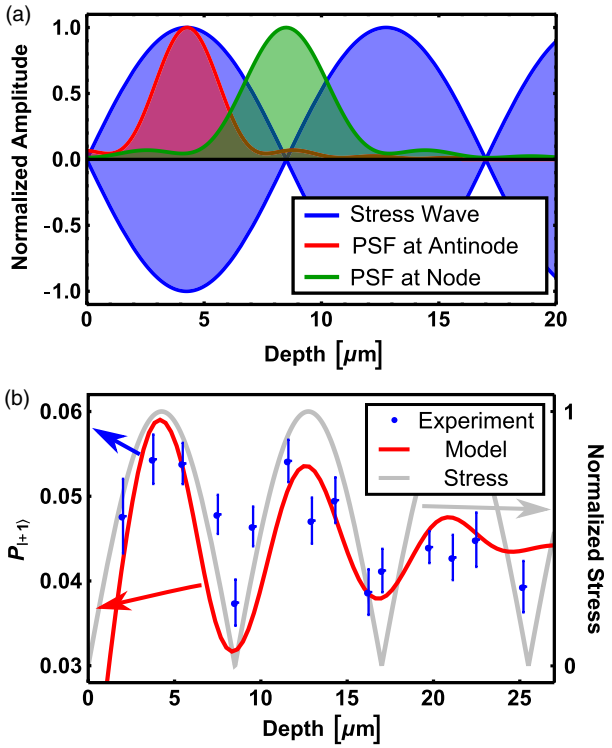

FIG. 3 (color online). (a) Normalized PSF of our confocal microscope plotted at a node and an antinode of the stress standing wave. (b) Peak ODMSR signal as a function of depth inside the diamond. The oscillations as a function of focal depth correspond to oscillations in stress along the standing wave used to drive spin transitions.

The ODMSR signal depends on the overlap between the oscillating stress and the PSF of the microscope, which is a maximum at an antinode of the stress standing wave. In contrast, ODMSR measured at a node is reduced by a factor of 1.5 [Fig. 3(b)]. Our approximate model, which is not a fit to the data, reproduces this ratio and the structure of the measured oscillation. To calculate the model curve, we convolve the stress standing wave with an approximated PSF that accounts for distortions in the position and shape of the PSF as a function of focal depth inside the diamond [26]. Crucially, we find excellent agreement between the spatial periodicity of the measured signal and the 17 μm wavelength of the HBAR-generated standing wave. This wavelength was calculated from the speed of sound in diamond (16 km/s) that we determined from the HBAR resonance pitch and the sample thickness. The decay of the measured oscillation at large depths is due to refractive aberration of the optical PSF, which increases linearly as a function of depth. Taken together, these observations are the "smoking gun" for mechanically driven spin transitions because the stress standing

wave is the only element of the experiment with spatial periodicity.

The modest ODMSR amplitudes of these measurements are limited by the amplitude of the stress wave, the power handling capabilities, and the driving field inhomogeneities in this first generation of devices. Because of these device limitations, we observe only incoherent driving of NV center spins. Improvements in device fabrication are estimated to increase the HBAR Qs by greater than a factor of 5 at room temperature [32], and cooling the samples to cryogenic temperature can increase the Q by a factor of $\approx 10^3$ [33]. Driving field inhomogeneities can be dispelled by driving either a single NV or a lateral plane of NVs, either of which would select a single value of the stress wave amplitude. Upon instituting these modest engineering improvements, we expect that coherent driving of the NV spin state is possible, putting stress driving on equal footing with magnetic driving.

Such control could have a number of practical sensing applications. Fang *et al.* demonstrated that using a $|\pm 1\rangle$ qubit for NV magnetometry enhances sensitivity and provides isolation from temperature fluctuations [6]. Because it directly couples the relevant states, mechanical driving could be useful for dynamical inversion of the $|\pm 1\rangle$ qubit, providing an alternative to $|\pm 1\rangle$ inversions constructed from a series of magnetic pulses that use $|0\rangle$ as a waypoint. Additionally, the spin signal from mechanically driven NV centers could be used as a precision sensor for gigahertz-frequency strains. One practical use may be to integrate NV centers with a MEMS accelerometer where acceleration shifts the intensity of ac strain. This would combine the high sensitivity of MEMS inertial sensing with the long-term stability of a spin transition, in a similar spirit to proposals for NV-based gyroscopes [34,35]. At low temperatures, it has been predicted that NV centers interacting with the cavity phonons of a mechanical resonator can generate a spin-squeezed state [1], and conversely, driven NV centers can be used to coherently cool or drive cavity phonons [17]. The mechanical spin driving presented here is the first step towards achieving these goals.

The development of new technology based on quantum spins in the solid state will depend on integration with both existing technology and other qubit systems. We have demonstrated spin manipulation through a direct interaction between spins and resonantly driven cavity phonons, thus, providing a new tool for integration and a new avenue for fundamental studies of spin-phonon interactions.

This work was supported by the Cornell Center for Materials Research with funding from the NSF MRSEC Program (No. DMR-1120296) and the Department of Energy Office of Science Graduate Fellowship Program (DOE SCGF), made possible in part by the American Recovery and Reinvestment Act of 2009, administered by ORISE-ORAU under Contract No. DE-AC05-06OR23100. Device fabrication was performed in part at the Cornell NanoScale Science and Technology Facility, a member of the National Nanotechnology Infrastructure Network, which is supported by the National Science Foundation (Grant No. ECCS-0335765).

*gdf9@cornell.edu

[1] S. D. Bennett, N. Y. Yao, J. Otterbach, P. Zoller, P. Rabl, and M. D. Lukin, Phys. Rev. Lett. **110**, 156402 (2013).
[2] A. Albrecht, A. Retzke, F. Jelezko, and M. B. Plenio, New J. Phys. **15**, 083014 (2013).
[3] H. Bernien, B. Hensen, W. Pfaff, G. Koolstra, M. S. Blok, L. Robledo, T. H. Taminiau, M. Markham, D. J. Twitchen, L. Childress, and R. Hanson, Nature (London) **497**, 86 (2013).
[4] L. Childress, M. V. Gurudev Dutt, J. M. Taylor, A. S. Zibrov, F. Jelezko, J. Wrachtrup, P. R. Hemmer, and M. D. Lukin, Science **314**, 281 (2006).
[5] P. Maletinsky, S. Hong, M. S. Grinolds, B. Hausmann, M. D. Lukin, R. L. Walsworth, M. Loncar, and A. Yacoby, Nat. Nanotechnol. **7**, 320 (2012).
[6] K. Fang, V. M. Acosta, C. Santori, Z. Huang, K. M. Itoh, H. Watanabe, S. Shikata, and R. G. Beausoleil, Phys. Rev. Lett. **110**, 130802 (2013).
[7] F. Dolde, H. Fedder, M. W. Doherty, T. Nöbauer, F. Rempp, G. Balasubramanian, T. Wolf, F. Reinhard, L. C. L. Hollenberg, F. Jelezko, and J. Wrachtrup, Nat. Phys. **7**, 459 (2011).
[8] D. M. Toyli, C. F. de las Casas, D. J. Christle, V. V. Dobrovitski, and D. D. Awschalom, Proc. Natl. Acad. Sci. U.S.A. **110**, 8417 (2013).
[9] G. Kucsko, P. C. Maurer, N. Y. Yao, M. Kubo, H. J. Noh, P. K. Lo, H. Park, and M. D. Lukin, Nature (London) **500**, 54 (2013).
[10] H. J. Mamin, M. Kim, M. H. Sherwood, C. T. Rettner, K. Ohno, D. D. Awschalom, and D. Rugar, Science **339**, 557 (2013).
[11] T. Staudacher, F. Shi, S. Pezzagna, J. Meijer, J. Du, C. A. Meriles, F. Reinhard, and J. Wrachtrup, Science **339**, 561 (2013).
[12] P. Rabl, S. J. Kolkowitz, F. H. L. Koppens, J. G. E. Harris, and P. Z. M. D. Lukin, Nat. Phys. **6**, 602 (2010).
[13] B. D'Urso, M. V. G. Dutt, S. Dhingra, and N. M. Nusran, New J. Phys. **13**, 045002 (2011).
[14] S. Kolkowitz, A. C. Bleszynski Jayich, Q. P. Unterreithmeier, S. D. Bennett, P. Rabl, J. G. E. Harris, and M. D. Lukin, Science **335**, 1603 (2012).
[15] S. Hong, M. S. Grinolds, P. Maletinsky, R. L. Walsworth, M. D. Lukin, and A. Yacoby, Nano Lett. **12**, 3920 (2012).
[16] P. Ovartchaiyapong, L. M. A. Pascal, B. A. Myers, P. Lauria, and A. C. B. Jayich, Appl. Phys. Lett. **101**, 163505 (2012).
[17] K. V. Kepesidis, S. D. Bennett, S. Portolan, M. D. Lukin, and P. Rabl, Phys. Rev. B **88**, 064105 (2013).
[18] V. V. Dobrovitski, G. D. Fuchs, A. L. Falk, C. Santori, and D. D. Awschalom, Annu. Rev. Condens. Matter Phys. **4**, 23 (2013).
[19] F. Jelezko, T. Gaebel, I. Popa, A. Gruber, and J. Wrachtrup, Phys. Rev. Lett. **92**, 076401 (2004).

[20] G. D. Fuchs, V. V. Dobrovitski, D. M. Toyli, F. J. Heremans, and D. D. Awschalom, Science **326**, 1520 (2009).
[21] C. G. Yale, B. B. Buckley, D. J. Christle, G. Burkard, F. J. Heremans, L. C. Bassett, and D. D. Awschalom, Proc. Natl. Acad. Sci. U.S.A. **110**, 7595 (2013).
[22] D. I. Bolef and R. K. Sundfors, *Nuclear Acoustic Resonance* (Acedemic, New York, 1993).
[23] M. W. Doherty, F. Dolde, H. Fedder, F. Jelezko, J. Wrachtrup, N. B. Manson, and L. C. L. Hollenberg, Phys. Rev. B **85**, 205203 (2012).
[24] E. Togan, Y. Chu, A. S. Trifonov, L. Jiang, J. Maze, L. Childress, M. V. G. Dutt, A. S. S. rensen, P. R. Hemmer, A. S. Zibrov, and M. D. Lukin, Nature (London) **466**, 730 (2010).
[25] K. M. Lakin, G. R. Kline, and K. T. McCarron, IEEE MTT-S Int. Microwave Symp. Dig. **3**, 1517 (1993).
[26] See Supplemental Material at http://link.aps.org/supplemental/10.1103/PhysRevLett.111.227602 for additional experimental details and calculations.
[27] D. A. Feld, R. Parker, R. Ruby, P. Bradley, and S. Dong, in *IEEE International Ultrasonics Symposium (IUS), Beijing, 2008* (IEEE, Piscataway, NJ, 2008), p. 431.
[28] K. F. Graff, *Wave Motion in Elastic Solids* (Dover, New York, 1991).
[29] C. P. Slicter, *Princples of Magnetic Resonance* (Springer, New York, 1990), 3rd ed.
[30] E. Vanoort and M. Glasbeek, Chem. Phys. Lett. **168**, 529 (1990).
[31] S. Hell, G. Reiner, C. Cremer, and E. H. K. Stelzer, J. Microsc. **169**, 391 (1993).
[32] B. P. Sorokin, G. M. Kvashnin, A. P. Volkov, V. S. Bormashov, V. V. Aksenenkov, M. S. Kuznetsov, G. I. Gordeev, and A. V. Telichko, Appl. Phys. Lett. **102**, 113507 (2013).
[33] T. Cheng, J. Hsiao, S. A. Bhave, and A. Duwel (to be published).
[34] A. Ajoy and P. Cappellaro, Phys. Rev. A **86**, 062104 (2012).
[35] M. P. Ledbetter, K. Jensen, R. Fischer, A. Jarmola, and D. Budker, Phys. Rev. A **86**, 052116 (2012).

Mechanical spin control of nitrogen-vacancy centers in diamond: Supplementary Information

E. R. MacQuarrie,[1] T. A. Gosavi,[1] N. R. Jungwirth,[1] S. A. Bhave,[1] and G. D. Fuchs[1,*]

[1] *Cornell University, Ithaca, NY 14853*

EXPERIMENTAL DETAILS

Measurements were performed using a home-built confocal microscope (Figure S1a). An Oxxius SLIM-532 150 mW laser was focused through a Gooch & Housego 15210 acousto-optic modulator (AOM) that was used as a high-speed shutter. An Optics in Motion 101 fast-scanning mirror was used to control the lateral position of the confocal focus. Both excitation and NV center emission were focused through an Olympus LMPLFLN, 100x objective. The emission was detected with an Excelitas SPCM-AQRH-FC avalanche photodiode.

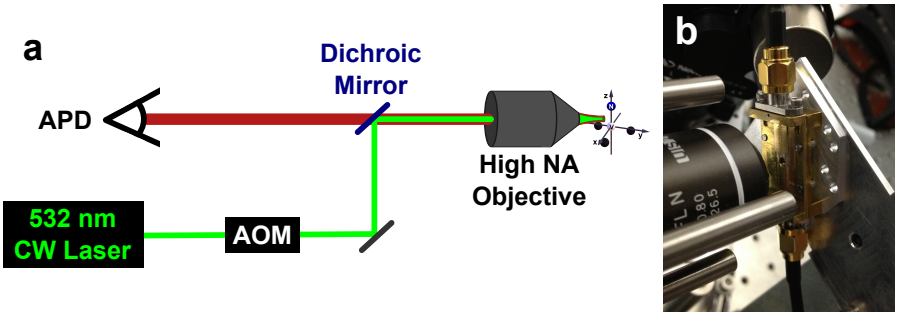

FIG. 1. (a) Home-built confocal microscope; (b) Diamond sample mounted in the microscope with custom-built brass sample box. The front side of the diamond (facing the microscope objective) has a lithographically-patterned microwave antenna wire bonded to a coplanar waveguide within the brass sample box. The back side contains the AlN transducer, which is wire-bonded to a second coplanar waveguide built into the brass sample box. Visible behind the brass sample box is the permanent magnet, which provides the static magnetic field in the experiment.

Samples were mounted in the custom-built brass sample box pictured in Figure S1b. The high-overtone bulk acoustic resonator (HBAR) device was powered by a Stanford Research Systems SG384 signal generator amplified by a Minicircuits ZRL-1150LN amplifier. The loop antenna was powered by a Tektronix 7122B Arbitrary Wave Generator (AWG) amplified by an Ophir 5161FE amplifier. A Stanford Research Systems DG645 digital delay generator triggered by the AWG was used to synchronize the various instruments and pulse the AOM. The axial magnetic field $B_{\|}$ was produced by a NdFeB permanent magnet on a motorized translation stage to enable field scanning.

The diamond substrate is an 'optical-grade,' 300μm thick, single-crystal diamond purchased from Element Six. The sample was first cleaned in a boiling nitric:sulfuric (3:2) acid

solution for one hour. Ti/Pt (25/225 nm) electrodes were then patterned on one face to serve as the ground plane for the HBARs. AlN was sputtered to a thickness of 3 μm, and an Al layer was patterned on top to serve as the HBAR signal electrode. The HBAR was then coated in photoresist for protection while Ti/Pt (25/225 nm) loop antennas were patterned on the opposite face.

MAGNETIC SPIN COHERENCE

The transverse magnetic spin coherence times were measured to be $T_2^* = 1.7 \pm 0.2$ μs and $T_2 = 100 \pm 30$ μs in the $|0\rangle \leftrightarrow |-1\rangle$ spin subspace using a Ramsey and Hahn echo sequence, respectively. The second $\pi/2$ pulse in our Ramsey sequence was phase delayed relative to the first $\pi/2$ pulse by $\phi = \Omega_{rot}(T_{\pi/2} + \tau)$ where $T_{\pi/2}$ is the length of a $\pi/2$ pulse. This detunes our measurement from the spin's rotating frame by Ω_{rot} and allows us to observe spin precession in the form of signal beating. All pulses in the Hahn echo measurement were phase continuous.

Pulse sequences and data for these measurements are presented in Figure 2. Inhomogeneities in the magnetic field reduce T_2^* in our sample—a typical signature of NV ensembles. The small discrepancies between the Ramsey data and our model are likely due to pulse errors or, more specifically, overlapping pulse tails, which create rotation and phase errors for short values of the inter-pulse delay τ. As demonstrated by Stanwix, *et al*, misalignment of our static magnetic field $B_{\|}$ may have reduced our measured T_2 from its optimum value [1].

ADIABATIC PASSAGE PARAMETERS

We used a linearly ramped adiabatic passage with $\Delta\omega = 100$ MHz detuning throughout our experiments. Because the amplitude of our magnetic driving field decreases at larger depths inside the diamond, the sweep rate of the adiabatic passage was optimized as a function of depth within the diamond to maintain fidelity. For measurements near the diamond surface, the adiabatic passage sweep rate was typically 31 MHz/μs. At the largest depths measured here (25 μm below the surface), the passage was 11.6 MHz/μs.

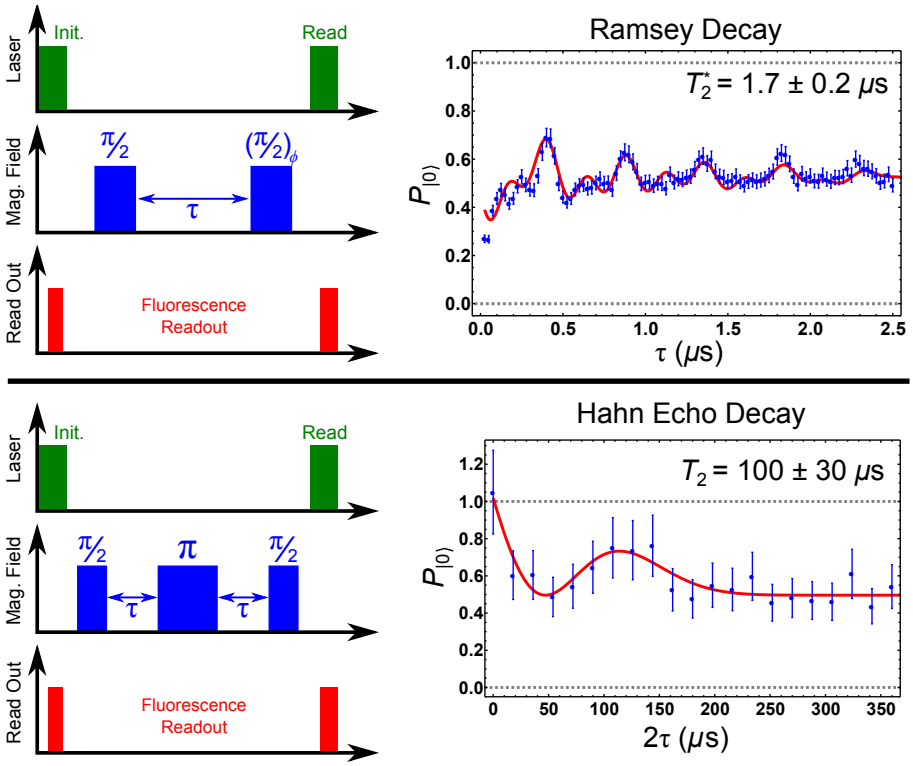

FIG. 2. Ramsey and Hahn echo measurements used to determine the magnetic spin coherence times of our NV center ensemble. Error bars are calculated from photon shot noise.

TREATMENT OF THE STRESS PROJECTION

In our mechanical spin driving experiments, we apply a $\approx$ 10 MPa stress along the [001] direction of the diamond lattice. This is described by the stress tensor in the lattice coordinate system

$$\mathbf{T} \approx \begin{pmatrix} 0 & 0 & 0 \\ 0 & 0 & 0 \\ 0 & 0 & 10 \end{pmatrix} \text{MPa} \tag{1}$$

We then transform $\mathbf{T}$ into the NV coordinate system defined such that the x', y', and z'-axes run along the $[\bar{1}\bar{1}2]$, $[1\bar{1}0]$, and$[111]$ lattice directions, respectively (Figure 3). This gives the stress tensor in the NV coordinates as

$$\mathbf{T}' \approx \begin{pmatrix} 7 & 0 & 5 \\ 0 & 0 & 0 \\ 5 & 0 & 3 \end{pmatrix} \text{MPa} \tag{2}$$

which corresponds to a $\approx$ 5 MPa shear stress and a $\approx$ 7 MPa normal stress along the x'-direction.

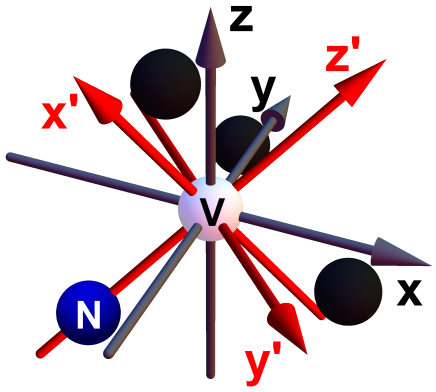

FIG. 3. Lattice coordinates (grey) and NV coordinates (red) used in the stress tensor analysis.

Although our experiment is performed in terms of stress, the NV center spin Hamiltonian is usually formulated to address strain [2]. Using the compliance matrix for diamond [3, 4], we convert $\mathbf{T}$ into a strain tensor $\mathbf{E}$ in the lattice coordinates:

$$\mathbf{E} \approx \begin{pmatrix} -5 & 0 & 0 \\ 0 & -5 & 0 \\ 0 & 0 & 90 \end{pmatrix} \times 10^{-7} \tag{3}$$

Transforming $\mathbf{E}$ into the NV coordinates, we find

$$\mathbf{E}' \approx \begin{pmatrix} 60 & 0 & 40 \\ 0 & -5 & 0 \\ 40 & 0 & 30 \end{pmatrix} \times 10^{-7} \tag{4}$$

which contains both shear strains and normal strains. As the torsional components of strain are usually neglected in derivations of the NV spin Hamiltonian [2], we neglect them here in both our strain and stress tensors, giving us $\sigma_\perp \approx 7$ MPa for the component of the stress perpendicular to the NV symmetry axis.

DRIVING FIELD CALIBRATION

We used conventional pulsed magnetic resonance signals to estimate the stress driving fields associated with the ODMSR signal. For calibration we modified the pulse sequence

shown in Figure 2a of the main text by replacing the stress pulse with a magnetic field pulse resonant with the $|-1\rangle \rightarrow |0\rangle$ spin transition. The population that was driven into the $|0\rangle$ state by this pulse was returned to the $|-1\rangle$ state during the second adiabatic passage, allowing us to observe magnetic spin driving as an absence of population in the $|0\rangle$ state.

We tuned the strength of the magnetic field pulse until the amplitude of the magnetic resonance signal matched that of our ODMSR signals. At this point, the driving fields generated by the stress pulse and the magnetic field pulse are equal, giving us a point of comparison. Because the magnetic driving field scales as $\sqrt{P}$ where P is the microwave power coupled into the loop antenna, we measured the magnetic driving field directly at a higher value of P by observing Rabi oscillations, and extrapolated downward to find the driving field generated by the weaker magnetic pulse.

To estimate the total driving amplitude of the ODMSR signals, we first subtract a constant background from the ODMSR signal that we attribute to pulse errors. By convolving the microscope PSF and the stress standing wave, we estimate that inhomogeneities in the stress driving field reduce the measured stress value to $0.84\sigma_{max}$ for the $\omega_{HBAR} = 2\pi \times 1.076$ GHz resonance at the anti-node closest to the diamond surface. Dividing the sum of the hyperfine peak amplitudes displayed in Figure 2b of the main text by this 0.84 correction factor gives the ideal peak ODMSR signal that we compare with our magnetic resonance data to determine a peak stress driving field of $\approx 2\pi \times 230$ kHz.

Using the approximate model described below, we determine the inhomogeneous mechanical driving of the NV ensemble reduces the observed ODMSR contrast by a factor of 1.2. Accounting for these effects, we estimate a 14% spin contrast for a single NV center with a polarized nuclear spin driven by an anti-node of the $\omega_{HBAR} = 2\pi \times 1.076$ GHz resonance.

HYPERFINE LEVEL ORDERING

The energy shifts resulting from hyperfine coupling with the ^{14}N nuclear spin are given by the expression

$$H_I = PI_z^2 + A_\parallel I_z S_z \tag{5}$$

where we use the hyperfine parameters $A_\parallel = -2.166$ MHz and $P = -4.945$ MHz [2, 5, 6]. Applying these energy shifts to the S_z eigenstates, we obtain the energy levels depicted in Figure 4, which match the ordering shown in Figure 2c of the main text.

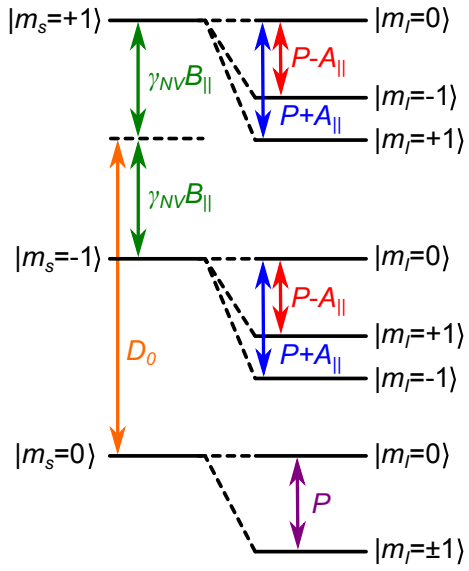

FIG. 4. Shifts to the electronic spin structure due to hyperfine coupling with the ^{14}N nuclear spin.

MEASUREMENTS AT DIFFERENT Q VALUES

Measurements were taken at two different stress resonances ($\omega_1 = 2\pi \times 1.076$ GHz and $\omega_2 = 2\pi \times 1.103$ GHz) which had Q's of 437 and 350 respectively. Since we are not driving the $|-1\rangle \rightarrow |+1\rangle$ spin transition to saturation, the stress driving field is expected to depend linearly on the Q of the resonance. To compare the driving field generated at different HBAR resonances, we take into account both the Q and the impedance of the HBAR for each resonance. The ratio of driving fields should match the ratio of stress, which may be calculated as

$$r_{stress} = \frac{Q_1}{Q_2} \times \frac{V_1}{V_2} = \frac{Q_1}{Q_2} \times \frac{Z_1\sqrt{50\ \Omega + Z_2}}{Z_2\sqrt{50\ \Omega + Z_1}} \tag{6}$$

where $Z_1 = 29.9\ \Omega$ is the microwave impedance of the HBAR at resonance 1 and $Z_2 = 33.5\ \Omega$ is the microwave impedance of the HBAR at resonance 2. Using the two resonances mentioned above, we measure the ratio of driving fields to be 1.10 ± 0.05, which is close to the expected value of $r_{stress} = 1.14$, which we calculate from equation S6 and network analyzer measurements.

RABI DRIVING WITH STRAIN

In order to determine the optimal pulse length for the stress wave in our measurements, we performed a Rabi-style ODMSR measurement where the length of the stress pulse τ was varied from 0 to a maximum value T. The pulse sequence for this experiment is depicted in Figure S5a. To mitigate thermal effects, the total power to the sample was kept constant by applying a buffer stress pulse of length $(T - \tau)$ after the second magnetic adiabatic passage (AP) has driven the $|-1\rangle$ population back into the $|0\rangle$ spin state. Because there is no magnetic pulse following this second stress pulse, population driven between $|+1\rangle$ to $|-1\rangle$ during the second pulse has no effect on fluorescence measurement, which is sensitive only to the population of $|0\rangle$.

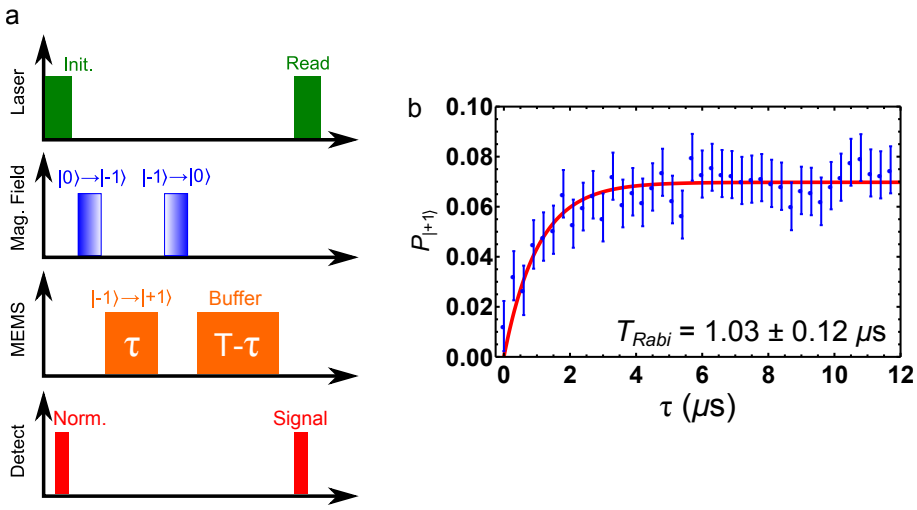

FIG. 5. (a) Pulse sequence for Rabi-style ODMSR measurement. The first MEMS pulse is for state transition, whereas the second pulse keeps the total MEMS power fixed throughout the duty cycle. The second pulse does not disturb the population of $|0\rangle$, which is proportional to the fluorescence contrast in spin measurement. (b) Results from Rabi-style ODMSR measurement. No coherent oscillations are observed because we measure fluorescence from inhomogeneous stresses within the confocal volume of our microscope.

The experimental signal, shown in Figure S5b, decays exponentially in τ. The characteristic decay time is $T_{Rabi} = 1.03 \pm 0.12$ μs, which we attribute to dephasing of the spin ensemble by inhomogeneous stress within the collection volume. From this measurement, we selected the 6 μs pulse length that was used for all of the ODMSR measurements reported

in the main text.

THE EFFECT OF STRAY MAGNETIC FIELDS FROM THE HBAR

We examined the effect of stray *magnetic* fields produced by the HBAR and resonant with the $|-1\rangle \leftrightarrow |+1\rangle$ transition, as a potential spurious contribution to the ODMSR signal. To understand this effect, we consider the Hamiltonian for an NV center in a static magnetic field that is aligned with the NV symmetry axis

$$H_0 = D_0 S_z^2 + \gamma_{NV} B_{\parallel} S_z, \tag{7}$$

with the perturbation

$$\Delta H = \gamma_{NV} B_{x0} S_x, \tag{8}$$

which represents a small ($B_{x0} \ll B_{\parallel}$) perpendicular component to the static magnetic field, aligned along the x-axis for simplicity.

To first order, ΔH mixes the eigenstates of H_0 without shifting their energy. Rewriting S_x in the basis defined by the first-order perturbed eigenstates, we find

$$S_x' = \begin{pmatrix} \frac{\gamma_{NV} B_{x0}}{\omega_{+1}} & \frac{1}{\sqrt{2}} & \frac{\gamma_{NV} B_{x0}}{2}\left(\frac{1}{\omega_{+1}} + \frac{1}{\omega_{-1}}\right) \\ \frac{1}{\sqrt{2}} & -\gamma_{NV} B_{x0}\left(\frac{1}{\omega_{+1}} + \frac{1}{\omega_{-1}}\right) & \frac{1}{\sqrt{2}} \\ \frac{\gamma_{NV} B_{x0}}{2}\left(\frac{1}{\omega_{+1}} + \frac{1}{\omega_{-1}}\right) & \frac{1}{\sqrt{2}} & \frac{\gamma_{NV} B_{x0}}{\omega_{-1}} \end{pmatrix}, \tag{9}$$

where we use ω_{+1} for the unperturbed $|0\rangle \rightarrow |+1\rangle$ transition energy and ω_{-1} for the unperturbed $|0\rangle \rightarrow |-1\rangle$ transition energy. This can be re-written as

$$S_x' = S_x + \frac{\gamma_{NV} B_{x0}}{2}\left(\frac{1}{\omega_{+1}} + \frac{1}{\omega_{-1}}\right)(S_x^2 - S_y^2) + \text{diagonal terms}. \tag{10}$$

The second term in S10 introduces transverse anisotropy with the same form as perpendicular stress. Therefore, application of a resonant oscillating field, $B_{x1}(t) = B_{x1}\cos[(\omega_{+1} - \omega_{-1})t]$ weakly drives spin transitions in a misaligned static magnetic field. Under the rotating wave approximation, the $|-1\rangle \leftrightarrow |+1\rangle$ driving field will be

$$\Omega_{|-1\rangle \rightarrow |+1\rangle} = \frac{\gamma_{NV}^2 B_{x1} B_{x0}}{4}\left(\frac{1}{\omega_{+1}} + \frac{1}{\omega_{-1}}\right) = \frac{\gamma_{NV}^2 B_{x1} B_{x0} D_0}{2(D_0^2 - \gamma_{NV}^2 B_{\parallel}^2)}. \tag{11}$$

Comparing this with the conventional expression for magnetically driving the $|0\rangle \rightarrow |\pm 1\rangle$ transition on resonance ($\Omega_{|0\rangle \rightarrow |\pm 1\rangle} = \gamma_{NV} B_{x1}/\sqrt{2}$), we find the following expression for the

ratio of driving fields:

$$\frac{\Omega_{|-1\rangle\rightarrow|+1\rangle}}{\Omega_{|0\rangle\rightarrow|\pm1\rangle}} = \frac{\sqrt{2}\gamma_{NV}B_{x0}D_0}{D_0^2 - \gamma_{NV}^2 B_{\|}^2}. \tag{12}$$

At $B_{\|} = 192$ G, this results in a driving field of $\Omega_{|-1\rangle\rightarrow|+1\rangle} \cong 0.0014 \times B_{x0} \times \Omega_{|0\rangle\rightarrow|\pm1\rangle}$, where B_{x0} has units of G.

As an experimental test of this effect, we replaced the stress wave pulse in our ODMSR experiments with a magnetic field pulse through the microwave antenna, resonant with the $|-1\rangle \rightarrow |+1\rangle$ transition, and with a power equivalent to $\Omega_{|0\rangle\rightarrow|\pm1\rangle} = 2\pi \times 820$kHz for conventional magnetic driving. Because we measured in a slightly misaligned magnetic field ($B_{x0} \neq 0$), we observed weak magnetic driving of the $|-1\rangle \rightarrow |+1\rangle$ transition. (Figure S6b).

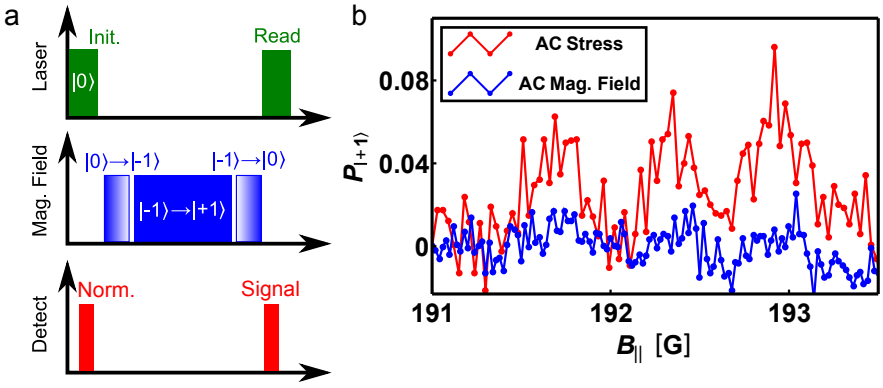

FIG. 6. (a) Pulse sequence for measuring B_{x1} field driving the $|-1\rangle \rightarrow |+1\rangle$ transition; (b) Magnetic driving of the $|-1\rangle \rightarrow |+1\rangle$ transition using $\Omega_{|0\rangle\rightarrow|\pm1\rangle} \approx 2\pi \times 820$kHz (blue) plotted next to stress driving (red). Both are measured on the $\omega_{HBAR} = 2\pi \times 1.076$ GHz acoustic resonance.

Using the electromagnetic simulation mentioned in the main text, we calculate that the stray magnetic field produced by the HBAR is $B_{1,HBAR} = 0.17$ G at the depth of optical measurements, and directed perpendicular to the plane. Under the most conservative estimate, we assume that $B_{x0} = 10$ G. Using equation S12, we estimate the stray magnetic field produces $\Omega_{|-1\rangle\rightarrow|+1\rangle} \cong 2\pi \times 2.7$ kHz, about 100× smaller than the stress-wave induced driving field. Moreover, this magnetic field is about 4× smaller than the field we applied in our experimental test, where we intentionally introduced a magnetic driving field through the microwave antenna. Interestingly, although we have just shown it is possible to drive the $|-1\rangle \leftrightarrow |+1\rangle$ spin transition magnetically, in most cases it is not practical. It requires

very large values of B_{x1} unless B_{x0} is sizable. Unfortunately, as B_{x0} grows, the eigenstates of the S_z basis mix more strongly, reducing both NV read-out contrast and spin coherence [1].

Magnetic driving of the $|-1\rangle \leftrightarrow |+1\rangle$ spin transition is fundamentally limited by weak coupling in the S_z basis, but mechanical driving is not, where the primary limitation is the stress wave amplitude. Mechanical driving affects neither spin coherence nor read-out contrast. With room temperature HBAR Q's expected to improve by more than a factor of five in the next generation of devices, mechanical driving is the more practical for route quantum control using the $|-1\rangle \leftrightarrow |+1\rangle$ spin transition.

CORRECTIONS TO THE PSF

To accurately interpret our measurement of the stress standing wave (Figure 3b of main text), it is critical to know the shape and location of our microscope's point spread function (PSF) inside the diamond. This problem is nontrivial because refraction at the air-diamond interface introduces aberrations that shift the focus deeper into the diamond and distort the PSF wavefront (Figure S7). Geometric optics relates the depth of the PSF inside the diamond d_{dia} to the nominal depth d_{air} as

$$d_{dia} = \frac{n_{dia}\cos\theta_{dia}}{n_{air}\cos\theta_{air}} d_{air} \tag{13}$$

where n is the index of refraction.

Assuming isotropic NV emission with intensity I_0, the power $P(\theta_{dia})$ that leaves the back of the objective is given by

$$P = \pi I_0 d_{dia}^2 \tan^2\theta_{dia} T(\theta_{dia}) \tag{14}$$

where $T(\theta_{dia})$ is the Fresnel transmission coefficient for unpolarized emission:

$$T(\theta_{dia}) = \frac{2n_{dia}n_{air}\cos\theta_{air}\cos\theta_{dia}}{(n_{dia}\cos\theta_{air} + n_{air}\cos\theta_{dia})^2} + \frac{2n_{dia}n_{air}\cos\theta_{air}\cos\theta_{dia}}{(n_{air}\cos\theta_{air} + n_{dia}\cos\theta_{dia})^2}. \tag{15}$$

We use Equation S13 and Snell's Law to express d_{dia} and θ_{air} as functions of θ_{dia}. Differentiating $P(\theta_{dia})$, we arrive at an expression for the differential power $\mathrm{d}P/\mathrm{d}\theta_{dia}$ that we use as a weight to determine the average value of d_{dia} as a function of d_{air}:

$$\langle d_{dia}\rangle = d_{air}\frac{\int_0^{\theta_{dia}^{max}} \frac{n_{dia}\cos\theta_{dia}}{n_{air}\cos\theta_{air}}\frac{\mathrm{d}P}{\mathrm{d}\theta_{dia}}\mathrm{d}\theta_{dia}}{\int_0^{\theta_{dia}^{max}}\frac{\mathrm{d}P}{\mathrm{d}\theta_{dia}}\mathrm{d}\theta_{dia}} \approx 3.2 d_{air} \tag{16}$$

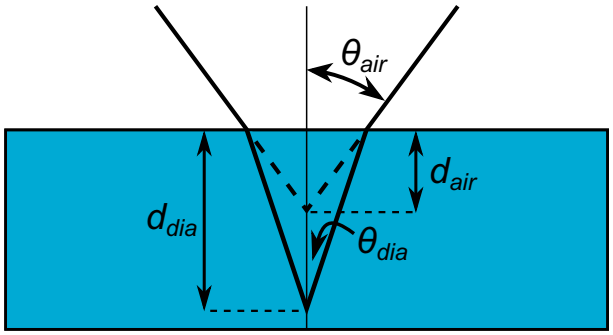

FIG. 7. (a) Geometry used to estimate the aberration introduced by refraction at the air-diamond interface.

where θ_{dia}^{max} is defined by the expression $\sin\theta_{dia}^{max} = \frac{\mathrm{NA}}{n_{dia}}$ and NA = 0.8.

This correction factor of 3.2 describes how the focal position shifts inside the diamond and serves as a lower bound to the true correction since we do not account for other aberrations in our microscope. For the wavelength of our measured standing wave to match the expected value of 17 μm, the correction factor needs to be 3.4 ± 0.1. We attribute the small mismatch in the wavelength to other aberrations, not accounted for in this calculation. The calculated 3.2 correction factor was used at all times in the main text.

In order to account for distortions to the shape of the PSF, we approximate the change in the PSF FWHM by the expression

$$FWHM_{dia} = \frac{1}{2}\left(\frac{n_{dia}\cos\theta_{dia}^{max}}{n_{air}\cos\theta_{air}^{max}} - \frac{n_{dia}\cos\theta_{dia}^{min}}{n_{air}\cos\theta_{air}^{min}}\right) d_{air} + FWHM_0 \tag{17}$$

where θ^{max} is set by the microscope NA and $\theta^{min} = 0$.

Measurements of single NV centers at shallow depths place $FWHM_0 \approx 2$ μm near the diamond surface. Using this as a starting point, we calculate the PSF near the surface using Fermat's principle which remains valid for high NA objectives [7]. We then propagate the PSF into the diamond using the approximate linear corrections to the PSF peak position and FWHM described above. By normalizing the resulting PSF, convolving it with a standing wave, and normalizing the result to the integrated area of the PSF, we produce the theoretical curve shown in Figure 3b of the main text. It is important to note that this is an approximation because it is not calculated using full diffraction theory and does not include non-refractive aberrations. Therefore, some differences between the model and the

experiment are expected.

---

* gdf9@cornell.edu

[1] Stanwix, P. L., Pham, L. M., Maze, J. R., Sage, D. L., Yeung, T. K., Cappellaro, P., Hemmer, P. R., Yacoby, A., Lukin, M. D., and Walsworth, R. L. *Phys. Rev. B* **82**(201201(R)) (2010).

[2] Doherty, M. W., Dolde, F., Fedder, H., Jelezko, F., Wrachtrup, J., Manson, N. B., and Hollenberg, L. C. L. *Phys. Rev. B* **85**(205203), 205203 (2012).

[3] Irgens, F. *Continuum Mechanics*. Springer, (2008).

[4] Klein, C. A. and Cardinale, G. F. *Diamond and Related Materials* **2**(57), 918 – 923 (1993).

[5] Smeltzer, B., McIntyre, J., and Childress, L. *Phys. Rev. A* **80**, 050302 Nov (2009).

[6] Steiner, M., Neumann, P., Beck, J., Jelezko, F., and Wrachtrup, J. *Phys. Rev. B* **81**, 035205 (2010).

[7] Hell, S., Reiner, G., Cremer, C., and Stelzer, E. H. K. *J. Microsc.* **169**(3), 391–405 (1993).